

Coupled multiphysics, barrier localization, and critical radius effects in embedded nanowire superlattices

Sanjay Prabhakar, Roderick Melnik, and Luis L Bonilla

Citation: *J. Appl. Phys.* **113**, 244306 (2013); doi: 10.1063/1.4812291

View online: <http://dx.doi.org/10.1063/1.4812291>

View Table of Contents: <http://jap.aip.org/resource/1/JAPIAU/v113/i24>

Published by the [AIP Publishing LLC](#).

Additional information on *J. Appl. Phys.*

Journal Homepage: <http://jap.aip.org/>

Journal Information: http://jap.aip.org/about/about_the_journal

Top downloads: http://jap.aip.org/features/most_downloaded

Information for Authors: <http://jap.aip.org/authors>

ADVERTISEMENT



**Running in Circles Looking
for the Best Science Job?**

Search hundreds of exciting
new jobs each month!

<http://careers.physicstoday.org/jobs>

physicstodayJOBS



Coupled multiphysics, barrier localization, and critical radius effects in embedded nanowire superlattices

Sanjay Prabhakar,^{1,a)} Roderick Melnik,^{1,2} and Luis L Bonilla²

¹M2NeT Laboratory, Wilfrid Laurier University, 75 University Avenue West, Waterloo, Ontario N2L 3C5, Canada

²Gregorio Millan Institute, Universidad Carlos III de Madrid, 28911 Leganes, Spain

(Received 7 February 2013; accepted 10 June 2013; published online 28 June 2013)

The new contribution of this paper is to develop a cylindrical representation of an already known multiphysics model for embedded nanowire superlattices (NWSLs) of wurtzite structure that includes a coupled, strain dependent 8-band $\mathbf{k} \cdot \mathbf{p}$ Hamiltonian in cylindrical coordinates and investigate the influence of coupled piezo-electromechanical effects on the barrier localization and critical radius in such NWSLs. The coupled piezo-electromechanical model for semiconductor materials takes into account the strain, piezoelectric effects, and spontaneous polarization. Based on the developed 3D model, the band structures of electrons (holes) obtained from results of modeling in Cartesian coordinates are in good agreement with those values obtained from our earlier developed 2D model in cylindrical coordinates. Several parameters such as lattice mismatch, piezo-electric fields, valence, and conduction band offsets at the heterojunction of $\text{Al}_x\text{Ga}_{1-x}\text{N}/\text{GaN}$ superlattice can be varied as a function of the Al mole fraction. When the band offsets at the heterojunction of $\text{Al}_x\text{Ga}_{1-x}\text{N}/\text{GaN}$ are very small and the influence of the piezo-electromechanical effects can be minimized, then the barrier material can no longer be treated as an infinite potential well. In this situation, it is possible to visualize the penetration of the Bloch wave function into the barrier material that provides an estimation of critical radii of NWSLs. In this case, the NWSLs can act as inversion layers. Finally, we investigate the influence of symmetry of the square and cylindrical NWSLs on the band structures of electrons in the conduction band. © 2013 AIP Publishing LLC. [<http://dx.doi.org/10.1063/1.4812291>]

I. INTRODUCTION

Studies on low dimensional systems, such as nanowires and superlattices, have attracted considerable attention, spurred on by the development of smaller and faster electronic devices and by the exploitation of their extraordinary properties for improved performance in various areas of science and technology, including nano- and micro-electronics, thermoelectricity, and magnetism.^{1–6} Today's technology allows finite length modulated quantum wire heterostructures to be grown in what is known as nanowire superlattices (NWSLs). NWSLs are the nanoscale building blocks that through the bottom up assembly can enable diverse applications. One can expect a straightforward analogy to the planar electronic/optoelectronic industry to extrapolate that complex compositionally modulated superlattice structures could greatly increase the versatility and power of these building blocks in nanoscale applications.⁷

In the NWSLs, the localization in barriers and the critical radius are important issues.^{8–10} The existence of barrier localization and the calculation of critical radius in NWSLs have been previously carried out by using one band effective mass theory in Refs. 11 and 12. Those earlier results indicated the possibility of these modulated structures to display free

carrier like behavior along the nanowire axis when a critical wire radius is considered. Moreover, it has been shown that the existence of critical radii for inversion of state localization is a much more general phenomenon. Most of these studies deal with free standing NWSLs. The barrier localization and critical radius phenomena can be particularly important in $\text{AlGaIn}/\text{GaIn}$ NWSLs where band structure parameters can be controlled with the variation of Al mole fraction. In this situation, the influence of piezo-electromechanical effects can be minimized. As a result, we see the penetration of the wavefunctions into the barrier materials which provides the evidence of the presence of critical radii in the NWSLs.^{11,13}

II. PIEZO-ELECTROMECHANICAL EFFECTS

A. Piezo-electromechanical effects in Cartesian coordinates

To investigate the influence of piezo-electromechanical effect on the band structure calculation of low dimensional semiconductor nanostructures, following Ref. 14, first we write the coupled system of the Navier equations for stress and Maxwell's equations for piezoelectric fields as^{15,16}

$$\partial_j \sigma_{ik} = 0, \quad (1)$$

$$\partial_i D_i = 0. \quad (2)$$

^{a)}sprabhakar@wlu.ca. URL: <http://www.m2netlab.wlu.ca>

The stress tensor components σ_{ik} and the electric displacement vector components D_i can be written as^{14,17}

$$\sigma_{ik} = C_{iklm}\epsilon_{lm} + e_{nik}\partial_n V, \quad (3)$$

$$D_i = e_{ilm}\epsilon_{lm} - \hat{\epsilon}_{in}\partial_n V + P_{sp}\delta_{iz}, \quad (4)$$

where C_{iklm} are the elastic moduli constants, e_{ik} is the piezoelectric constant, ϵ_{in} is the permittivity, V is the piezoelectric potential, P_{sp} is the spontaneous polarization, and V is the built in piezoelectric potential. Also, ϵ_{ik} are the components of strain tensors which are written as

$$\epsilon_{ij} = \epsilon_{ij}^u + \epsilon_{ij}^0, \quad (5)$$

where ϵ_{ij}^0 are the local intrinsic strain tensor components due to lattice mismatch and ϵ_{ij}^u is position dependent strain tensor components. These two can be written as

$$\epsilon_{ij}^0 = (\delta_{ij} - \delta_{iz}\delta_{jz})a + \delta_{iz}\delta_{jz}c, \quad (6)$$

$$\epsilon_{ij}^u = \frac{1}{2}(\partial_j u_i + \partial_i u_j), \quad (7)$$

where $a = (a_0 - a)/a_0$ and $c = (c_0 - c)/c_0$ are the local intrinsic strains along a - and c -directions, respectively (which are nonzero in the quantum well (QW) and zero otherwise). Here, a_0 , c_0 and a , c are the lattice constants of the quantum well and the barrier material of the NWLSs.

B. Piezo-electromechanical effects in cylindrical coordinates

In cylindrical polar coordinates (r, ϕ, z) , Eqs. (3) and (4) can be written as^{15,17–19}

$$\sigma_{rr} = C_{11}\epsilon_{rr} + C_{12}\epsilon_{\phi\phi} + C_{13}\epsilon_{zz} + e_{31}\partial_z V, \quad (8)$$

$$\sigma_{\phi\phi} = C_{11}\epsilon_{\phi\phi} + C_{12}\epsilon_{rr} + C_{13}\epsilon_{zz} + e_{31}\partial_z V, \quad (9)$$

$$\sigma_{rz} = 2C_{44}\epsilon_{rz} + e_{15}\partial_r V, \quad (10)$$

$$\sigma_{zz} = C_{13}\epsilon_{rr} + C_{13}\epsilon_{\phi\phi} + C_{33}\epsilon_{zz} + e_{33}\partial_z V, \quad (11)$$

$$D_r = 2e_{15}\epsilon_{rz} - \epsilon_1\partial_r V, \quad (12)$$

$$D_z = e_{31}(\epsilon_{rr} + \epsilon_{\phi\phi}) + e_{33}\epsilon_{zz} - \epsilon_3\partial_z V + P_z^{sp}. \quad (13)$$

Also, the coupled equations of wurtzite structure in the presence of piezo-electromechanical effects in cylindrical coordinates can be written as¹⁵

$$\partial_r \sigma_{rr} + \partial_z \sigma_{rz} + \frac{\sigma_{rr} - \sigma_{\phi\phi}}{r} = 0, \quad (14)$$

$$\partial_r \sigma_{rz} + \partial_z \sigma_{zz} + \frac{1}{r}\sigma_{rz} = 0, \quad (15)$$

$$\partial_r D_r + \partial_z D_z + \frac{1}{r}D_r = 0. \quad (16)$$

From Eqs. (8) to (13), the components of the strain tensor, expressed through the displacement vector $\mathbf{u} = (u_r, u_\phi, u_z)$, for which $\partial_\phi \mathbf{u} = 0$, are

$$\epsilon_{rr} = \partial_r u_r + a, \quad \epsilon_{zz} = \partial_z u_z + c, \quad (17)$$

$$\epsilon_{\phi\phi} = \frac{u_r}{r} + a, \quad \epsilon_{rz} = \frac{1}{2}(\partial_z u_r + \partial_r u_z). \quad (18)$$

The strain tensor components and the piezoelectric field (potential) can be found by solving the electroelasticity problem (14)–(16).

III. BAND STRUCTURE CALCULATIONS

A. 8-band $\mathbf{k} \cdot \mathbf{p}$ model in Cartesian coordinates

The steady state Schrödinger equation of the Kane model for the electrons in the conduction band and holes in the valence band can be written as^{16,20–24}

$$\mathbf{H}\psi = E\psi, \quad (19)$$

where

$$\mathbf{H} = \begin{pmatrix} \mathbf{H}_c & \mathbf{H}_{cv} \\ \mathbf{H}_{cv}^\dagger & \mathbf{H}_v \end{pmatrix}, \quad \psi = \begin{pmatrix} \psi_c \\ \psi_v \end{pmatrix}, \quad (20)$$

with $\psi_c = \psi_c(\mathbf{r})$ and $\psi_v = \psi_v(\mathbf{r})$ are the position dependent conduction and valence band envelope functions.

The total wave function Ψ is^{16,25}

$$\Psi = \sum_{j=c,x,y,z} f_j \psi_j = \mathbf{f}\psi, \quad (21)$$

where $\mathbf{f} = (f_c, f_x, f_y, f_z)$ and $\psi = (\psi_c, \psi_x, \psi_y, \psi_z)^T$. The functions \mathbf{f} are spinless and ψ is a spinor

$$\psi_j = \begin{pmatrix} \psi_j^1 \\ \psi_j^2 \end{pmatrix}, \quad j = c, x, y, z. \quad (22)$$

Hence, the basis functions of the Hamiltonian (20) take the following form:^{16,25}

$$(f_c\psi_c^1, f_c\psi_c^2, f_x\psi_x^1, f_x\psi_x^2, f_y\psi_y^1, f_y\psi_y^2, f_z\psi_z^1, f_z\psi_z^2)^T.$$

We now turn to the description of the matrix Hamiltonian \mathbf{H} of Eq. (20). The diagonal element of the conduction band Hamiltonian \mathbf{H}_c can be written as

$$H_c = A_1'k_z^2 + A_2'(k_x^2 + k_y^2) + U_c + a_1\epsilon_{zz} + a_2(\epsilon_{xx} + \epsilon_{yy}), \quad (23)$$

where $U_c = U_c(\mathbf{r})$ is the position dependent edge of the conduction band Γ_1 , a_1 and a_2 are deformation potentials for the conduction band. The parameters A_1' and A_2' are expressed via the components $1/m_{\parallel}$ and $1/m_{\perp}$ of the tensor of the reciprocal effective masses for the conduction band in

the single-band approximation and the Kane parameters $P_1 = -i\hbar\langle\phi_c|\hbar k_z|\phi_z\rangle/m_0$ and $P_2 = -i\hbar\langle\phi_c|\hbar k_x|\phi_x\rangle/m_0$. They are given by^{16,25}

$$A'_1 = \frac{\hbar^2}{2m_{\parallel}} - \frac{P_1^2}{E_g}, \quad (24)$$

$$A'_2 = \frac{\hbar^2}{2m_{\perp}} - \frac{P_2^2}{E_g}, \quad (25)$$

where E_g is the band gap of semiconductor materials.

The intra-valence-band Hamiltonian \mathbf{H}_v can be written as

$$\mathbf{H}_v = \mathbf{H}^{(0)} + \mathbf{H}^{(\text{so})} + \mathbf{H}^{(z)} + \mathbf{H}^{(\mathbf{k})}. \quad (26)$$

The Hamiltonian $\mathbf{H}^{(0)}$ entering Eq. (26) represents the position-dependent potential energy of an electron

$$\mathbf{H}^{(0)} = \begin{pmatrix} U_{v6} & 0 & 0 \\ 0 & U_{v6} & 0 \\ 0 & 0 & U_{v1} \end{pmatrix}, \quad (27)$$

where $U_{v6} = U_{v6}(\mathbf{r})$ and $U_{v1} = U_{v1}(\mathbf{r})$ are the position dependent edges of the valence bands Γ_6 and Γ_1 , respectively.

The spin-orbit Hamiltonian $\mathbf{H}^{(\text{so})}$ in Eq. (26) can be treated as a perturbation term and can be written as^{21,26}

$$\mathbf{H}^{(\text{so})} = i \begin{pmatrix} 0 & -\Delta_2\sigma_z & \Delta_3\sigma_y \\ \Delta_2\sigma_z & 0 & -\Delta_3\sigma_x \\ -\Delta_3\sigma_y & \Delta_3\sigma_x & 0 \end{pmatrix}, \quad (28)$$

where $\Delta_2 = \Delta_2(\mathbf{r})$ and $\Delta_3 = \Delta_3(\mathbf{r})$ are the parameters of the valence-band spin-orbit splitting and σ_i ($i = x, y, z$) are the Pauli spin matrices

$$\sigma_x = \begin{pmatrix} 0 & 1 \\ 1 & 0 \end{pmatrix}, \quad \sigma_y = \begin{pmatrix} 0 & -i \\ i & 0 \end{pmatrix}, \quad \sigma_z = \begin{pmatrix} 1 & 0 \\ 0 & -1 \end{pmatrix}. \quad (29)$$

The kinetic energy Hamiltonian $\mathbf{H}^{(\mathbf{k})}$ in Eq. (26) can be written as²⁵

$$\mathbf{H}^{(\mathbf{k})} = \begin{pmatrix} L'_1 k_x^2 + M_1 k_y^2 + M_2 k_z^2 & N'_1 k_x k_y & N'_2 k_x k_z \\ N'_1 k_x k_y & M_1 k_x^2 + L'_1 k_y^2 + M_2 k_z^2 & N'_2 k_y k_z \\ N'_2 k_x k_z & N'_2 k_y k_z & M_3(k_x^2 + k_y^2) + L'_2 k_z^2 \end{pmatrix}, \quad (30)$$

where

$$L'_1 = L_1 + \frac{P_1^2}{E_g}, \quad L'_2 = L_2 + \frac{P_2^2}{E_g}, \quad (31)$$

$$N'_1 = N_1 + \frac{P_1^2}{E_g}, \quad N'_2 = N_2 + \frac{P_1 P_2}{E_g}. \quad (32)$$

Also,

$$\begin{aligned} L_1 &= \frac{\hbar^2}{2m_0} (A_2 + A_4 + A_5), \\ M_1 &= \frac{\hbar^2}{2m_0} (A_2 + A_4 - A_5), \\ N_1 &= \frac{\hbar^2}{2m_0} 2A_5, \quad L_2 = \frac{\hbar^2}{2m_0} A_1, \\ M_2 &= \frac{\hbar^2}{2m_0} (A_1 + A_3), \quad N_2 = \frac{\hbar^2}{2m_0} \sqrt{2}A_6, \\ M_3 &= \frac{\hbar^2}{2m_0} A_2, \quad N_3 = i\sqrt{2}A_7, \end{aligned} \quad (33)$$

with A_1, A_2, \dots, A_7 being real material parameters in conventional notations,^{21,25,26} m_0 is the free electron mass. Wurtzite structure has six fold rotational symmetry and thus we use the relation $L'_1 - M_1 = N'_1$.

Finally, the strain tensor components are written as²⁷

$$\mathbf{H}^{(z)} = \begin{pmatrix} l_1 \varepsilon_{xx} + m_1 \varepsilon_{yy} + m_2 \varepsilon_{zz} & n_1 \varepsilon_{xy} & n_2 \varepsilon_{xz} \\ n_1 \varepsilon_{xy} & m_1 \varepsilon_{xx} + l_1 \varepsilon_{yy} + m_2 \varepsilon_{zz} & n_2 \varepsilon_{yz} \\ n_2 \varepsilon_{xz} & n_2 \varepsilon_{yz} & m_3 (\varepsilon_{xx} + \varepsilon_{yy}) + l_2 \varepsilon_{zz} \end{pmatrix}, \quad (34)$$

where material constants l_1 , l_2 , m_1 , m_2 , n_1 , and n_2 are expressed via conventional deformation potential tensor components as follows:^{21,25,26}

$$\begin{aligned} l_1 &= D_2 + D_4 + D_5, & m_1 &= D_2 + D_4 - D_5, \\ n_1 &= 2D_5, & l_2 &= D_1, & m_2 &= D_1 + D_3, \\ n_2 &= \sqrt{2}D_6, & m_3 &= D_2. \end{aligned} \quad (35)$$

We can also apply six fold rotational symmetry in the strain Hamiltonian of wurtzite structure which holds the relation $l_1 - m_1 = n_1$.

The Hamiltonian \mathbf{H}_{cv} of (20) ($\mathbf{H}_{\text{cv}}^\dagger$ is its Hermitian conjugate) can be written as

$$\mathbf{H}_{\text{cv}} = \begin{pmatrix} H_{cx} & H_{cy} & H_{cz} \end{pmatrix}, \quad (36)$$

where

$$H_{cx} = iP_2k_x, \quad H_{cy} = iP_2k_y, \quad H_{cz} = iP_1k_z. \quad (37)$$

B. 8-band $\mathbf{k} \cdot \mathbf{p}$ model in cylindrical coordinates

To derive the strain dependent 8-band $\mathbf{k} \cdot \mathbf{p}$ model in cylindrical coordinates (r, z), with $x = r \cos \phi$ and $y = r \sin \phi$, we introduce two different unitary matrix as^{28,31}

$$\mathbf{S}_1 = \begin{pmatrix} 1 & 0 & 0 & 0 \\ 0 & \cos \phi & \sin \phi & 0 \\ 0 & -\sin \phi & \cos \phi & 0 \\ 0 & 0 & 0 & 1 \end{pmatrix}, \quad (38)$$

$$\mathbf{S}_2 = \begin{pmatrix} e^{i\frac{\phi}{2}\sigma_z} & 0 & 0 & 0 \\ 0 & e^{i\frac{\phi}{2}\sigma_z} & 0 & 0 \\ 0 & 0 & e^{i\frac{\phi}{2}\sigma_z} & 0 \\ 0 & 0 & 0 & e^{i\frac{\phi}{2}\sigma_z} \end{pmatrix}. \quad (39)$$

We rotate the strain dependent 8-band $\mathbf{k} \cdot \mathbf{p}$ Hamiltonian (19) by $\tilde{\mathbf{H}} = \mathbf{S}_2 \mathbf{S}_1 \mathbf{H} \mathbf{S}_1^{-1} \mathbf{S}_2^{-1}$. We follow here the ideas first published in Refs. 28 and 29. Thus, the eigenvalue problem (19) can be written as

$$\tilde{\mathbf{H}} \tilde{\psi} = E \tilde{\psi}. \quad (40)$$

In Eq. (40), we introduce new basis functions $\tilde{\mathbf{f}} = (f_c, f_r, f_\phi, f_z)$, where

$$f_r = \frac{xf_x + yf_y}{\sqrt{x^2 + y^2}}, \quad f_\phi = \frac{xf_y - yf_x}{\sqrt{x^2 + y^2}}. \quad (41)$$

Note that the new basis functions are invariant under the rotation of the Cartesian coordinate system around the

z-axis, i.e., $\mathbf{f} = \tilde{\mathbf{f}} \mathbf{S}_1$. It can be seen that f_r and f_ϕ do not obey the periodicity properties of the functions f_x and f_y and thus they are not the Bloch functions at this moment. The total wavefunction Ψ and the envelope functions $\tilde{\psi}$ are related to each other through conventional basis functions \mathbf{f} or the modified functions $\tilde{\mathbf{f}}$ ($\mathbf{f} = \tilde{\mathbf{f}} \mathbf{S}_1$) as follows:

$$\Psi = \mathbf{f} \mathbf{S}_1^{-1} \mathbf{S}_2^{-1} \tilde{\psi} = \tilde{\mathbf{f}} \mathbf{S}_2^{-1} \tilde{\psi}. \quad (42)$$

Earlier we have noticed that f_r and f_ϕ are not periodic and they are not Bloch functions so it is convenient to retain the old basis functions \mathbf{f} which are periodic and orthonormal. Thus, we obtain the old envelope functions ψ as

$$\psi = \mathbf{S}_1^{-1} \mathbf{S}_2^{-1} \tilde{\psi}. \quad (43)$$

To transform the Hamiltonian (20) ($\tilde{\mathbf{H}} = \mathbf{S}_2 \mathbf{S}_1 \mathbf{H} \mathbf{S}_1^{-1} \mathbf{S}_2^{-1}$), we use the following identities:

$$\begin{aligned} \partial_x &= \cos \phi \partial_r - \frac{\sin \phi}{r} \partial_\phi, \\ \partial_y &= \sin \phi \partial_r + \frac{\cos \phi}{r} \partial_\phi, \end{aligned} \quad (44)$$

as well as the relations

$$\begin{aligned} \varepsilon_{xx} &= \varepsilon_{rr} \cos^2 \phi + \varepsilon_{\phi\phi} \sin^2 \phi - \varepsilon_{r\phi} \sin 2\phi, \\ \varepsilon_{yy} &= \varepsilon_{rr} \sin^2 \phi + \varepsilon_{\phi\phi} \cos^2 \phi + \varepsilon_{r\phi} \sin 2\phi, \\ \varepsilon_{xy} &= \frac{\varepsilon_{rr} - \varepsilon_{\phi\phi}}{2} \sin 2\phi + \varepsilon_{r\phi} \cos 2\phi, \\ \varepsilon_{xz} &= \varepsilon_{rz} \cos \phi - \varepsilon_{\phi z} \sin \phi, \\ \varepsilon_{yz} &= \varepsilon_{rz} \sin \phi + \varepsilon_{\phi z} \cos \phi. \end{aligned} \quad (45)$$

We obtain the elements of $\tilde{\mathbf{H}} = \mathbf{S}_1 \mathbf{H} \mathbf{S}_1^{-1}$ (see Eq. (30)) as follows:

$$\begin{aligned} \tilde{H}_c &= -A'_1 \partial_z^2 - A'_2 \left(\partial_r^2 - \frac{1}{r^2} \partial_\phi^2 - \frac{1}{r} \partial_r \right) + U_c \\ &+ a_1 \varepsilon_{zz} + a_2 (\varepsilon_{rr} + \varepsilon_{\phi\phi}), \end{aligned} \quad (46)$$

$$\begin{aligned} \tilde{H}_{11}^{(k)} &= \cos \phi H_{11}^{(k)} \cos \phi + \cos \phi H_{21}^{(k)} \sin \phi \\ &+ \sin \phi H_{12}^{(k)} \cos \phi + \sin \phi H_{22}^{(k)} \sin \phi \\ &= -L_1 \left(\partial_r^2 + \partial_r \frac{1}{r} \right) - M_1 \frac{1}{r^2} \partial_\phi^2 - M_2 \partial_z^2, \end{aligned} \quad (47)$$

$$\begin{aligned} \tilde{H}_{12}^{(k)} &= -\cos \phi H_{11}^{(k)} \sin \phi + \cos \phi H_{21}^{(k)} \cos \phi \\ &- \sin \phi H_{12}^{(k)} \sin \phi + \sin \phi H_{22}^{(k)} \cos \phi \\ &= -L_1 \partial_r \frac{1}{r} \partial_\phi + M_1 \left(\frac{1}{r} \partial_r \partial_\phi + \frac{1}{r^2} \partial_\phi \right). \end{aligned} \quad (48)$$

The rest of the elements are obtained analogously. Thus, the full matrix of the kinetic energy Hamiltonian (30) in the rotated frame $\tilde{\mathbf{H}} = \mathbf{S}_1 \mathbf{H} \mathbf{S}_1^{-1}$ can be written as

$$\tilde{\mathbf{H}}^{(k)} = - \begin{pmatrix} L_1 \left[\partial_r^2 + \partial_r \frac{1}{r} \right] + M_1 \frac{\partial_\phi^2}{r^2} + M_2 \partial_z^2 & L_1 \partial_r \frac{\partial_\phi}{r} - M_1 \left[\frac{\partial_\phi}{r} \partial_r + \frac{\partial_\phi}{r^2} \right] & N_2 \partial_r \partial_z \\ L_1 \left[\frac{\partial_\phi}{r} \partial_r + \frac{\partial_\phi}{r^2} \right] - M_1 \partial_r \frac{\partial_\phi}{r} & M_1 \left[\partial_r^2 + \partial_r \frac{1}{r} \right] + L_1 \frac{\partial_\phi^2}{r^2} + M_2 \partial_z^2 & N_2 \frac{\partial_\phi}{r} \partial_z \\ N_2 \left[\partial_r + \frac{1}{r} \right] \partial_z & N_2 \frac{\partial_\phi}{r} \partial_z & M_3 \left[\partial_r^2 + \frac{1}{r} \partial_r + \frac{\partial_\phi^2}{r^2} \right] + L_2 \partial_z^2 \end{pmatrix}. \quad (49)$$

Note that $\partial_r^T = -(\partial_r + r^{-1})$ and thus the Hamiltonian (49) is Hermitian. It can be seen that Hamiltonian (49) resembles the one in Refs. 29 and 30 with different coefficients due to the fact that our choice of the basis functions and unitary rotation matrix are different. Since $\tilde{\mathbf{H}}^{(so)} = \mathbf{S}_1 \mathbf{H}_{so} \mathbf{S}_1^{-1}$ (see Eq. (54)) will contain ϕ that does not commute with the operator $-i\partial_\phi$, we need to perform another set of rotation $\tilde{\mathbf{H}}^{(so)} = \mathbf{S}_2 \tilde{\mathbf{H}} \mathbf{S}_2^{-1}$ to remove the ϕ dependency from $\tilde{\mathbf{H}}^{(so)}$. Thus, it is also required to find all the elements of $\tilde{\mathbf{H}} = \mathbf{S}_1 \mathbf{H} \mathbf{S}_1^{-1}$ under the rotation $\tilde{\mathbf{H}} = \mathbf{S}_2 \tilde{\mathbf{H}} \mathbf{S}_2^{-1}$. Again, by performing another lengthy algebraic transformations, we obtain the elements of $\tilde{\mathbf{H}} = \mathbf{S}_2 \tilde{\mathbf{H}} \mathbf{S}_2^{-1}$ (see Eq. (20)). For example, \tilde{H}_c of Eq. (23) can be written as

$$\begin{aligned} \tilde{H}_c = & -A'_1 \partial_z^2 - A'_2 \left(\partial_r^2 - \frac{1}{r^2} \hat{\partial}_\phi^2 - \frac{1}{r} \partial_r \right) + U_c + a_1 \varepsilon_{zz} \\ & + a_2 (\varepsilon_{rr} + \varepsilon_{\phi\phi}), \end{aligned} \quad (50)$$

where we use the identity

$$\begin{aligned} \hat{\partial}_\phi &= e^{i\frac{\phi}{2}\sigma_z} \partial_\phi e^{-i\frac{\phi}{2}\sigma_z} = \partial_\phi - \frac{i}{2} \sigma_z \\ &= \begin{pmatrix} \partial_\phi - \frac{i}{2} & 0 \\ 0 & \partial_\phi + \frac{i}{2} \end{pmatrix}. \end{aligned} \quad (51)$$

Similarly, \tilde{H}_{cx} of Eq. (37) can be written as

$$\tilde{H}_{cx} = P_2 \left(\partial_r + \frac{1}{r} \right). \quad (52)$$

Also, first element of $\tilde{\mathbf{H}}^k = \mathbf{S}_2 \mathbf{S}_1 \mathbf{H}^k \mathbf{S}_1^{-1} \mathbf{S}_2^{-1}$ in Eq. (30) can be written as

$$\tilde{\mathbf{H}}_{11}^k = -L_1 \left(\partial_r^2 + \partial_r \frac{1}{r} \right) - M_1 \frac{1}{r^2} \hat{\partial}_\phi^2 - M_2 \partial_z^2. \quad (53)$$

In a similar fashion, one can find the rest of the elements of strain dependent 8-band $\mathbf{k} \cdot \mathbf{p}$ Hamiltonian in cylindrical

polar coordinates (r, ϕ, z) . The results of this procedure were first reported in Ref. 28 and 29.

Following it, we can transform the spin-orbit interaction Hamiltonian (28) as $\tilde{\mathbf{H}}^{(so)} = \mathbf{S}_2 \tilde{\mathbf{H}}^{(so)} \mathbf{S}_2^{-1}$, where $\tilde{\mathbf{H}}^{(so)} = \mathbf{S}_1 \mathbf{H}^{(so)} \mathbf{S}_1^{-1}$. Thus, we can write

$$\tilde{\mathbf{H}}^{(so)} = i \begin{pmatrix} 0 & -\Delta_2 \sigma_z & \Delta_3 \sigma_\phi \\ \Delta_2 \sigma_z & 0 & -\Delta_3 \sigma_r \\ -\Delta_3 \sigma_\phi & \Delta_3 \sigma_r & 0 \end{pmatrix}, \quad (54)$$

where $\sigma_r = \sigma_x \exp(i\phi\sigma_z)$ and $\sigma_\phi = \sigma_y \exp(i\phi\sigma_z)$.

Notice that the spin-orbit Hamiltonian (54) depends on ϕ which does not commute with the operator $-i\partial_\phi$. To avoid this dependence, we note that

$$e^{i\frac{\phi}{2}\sigma_z} \sigma_r e^{-i\frac{\phi}{2}\sigma_z} = \sigma_x, \quad e^{i\frac{\phi}{2}\sigma_z} \sigma_\phi e^{-i\frac{\phi}{2}\sigma_z} = \sigma_y, \quad (55)$$

and then the spin-orbit interaction Hamiltonian $\tilde{\mathbf{H}}^{(so)}$ transforms into its initial form (28)

$$\tilde{\mathbf{H}}^{(so)} = \mathbf{S}_2 \tilde{\mathbf{H}}^{(so)} \mathbf{S}_2^{-1} = \mathbf{H}^{(so)}. \quad (56)$$

For cylindrically symmetric systems, the total rotated Hamiltonian $\tilde{\mathbf{H}}$ commutes with the z-component of the total angular momentum operator $j_z = -i\hbar\partial_\phi$. These two commuting operators have the common eigenfunctions so that the total rotated envelope functions can be chosen in the form of

$$\tilde{\psi} = \frac{e^{im\phi}}{\sqrt{2\pi}} \psi(r, z), \quad (57)$$

where $m = \pm 1/2, \pm 3/2, \dots$ are the eigenvalues of the z-components of the total angular momentum j_z . The advantage of using these basis functions (57) in the rotated frame is that the total Hamiltonian becomes ϕ independent from the strain dependent 8-band $\mathbf{k} \cdot \mathbf{p}$ Hamiltonian.

Now, we summarize the strain dependent 8-band $\mathbf{k} \cdot \mathbf{p}$ Hamiltonian in cylindrical coordinates as follows:

$$\tilde{\mathbf{H}} = \begin{pmatrix} \begin{pmatrix} -A'_2 \left(\partial_r^2 - \frac{\mathbf{m}^2}{r^2} - \frac{1}{r} \partial_r \right) \\ -A'_1 \partial_z^2 + U_c + a_1 \varepsilon_{zz} \\ + a_2 (\varepsilon_{rr} + \varepsilon_{\phi\phi}) \end{pmatrix} \hat{\mathbf{i}} & \hat{\mathbf{i}} P_2 \left(\partial_r + \frac{1}{r} \right) & \frac{imP_2}{r} & \hat{\mathbf{i}} P_1 \partial_z \\ -\hat{\mathbf{i}} P_2 \partial_r & \begin{pmatrix} -L'_1 \left[\partial_r^2 + \partial_r \frac{1}{r} \right] \\ + M_1 \frac{\mathbf{m}^2}{r^2} - M_2 \partial_z^2 \\ + U_{v6} + l_1 \varepsilon_{rr} \\ + m_1 \varepsilon_{\phi\phi} + m_2 \varepsilon_{zz} \end{pmatrix} \hat{\mathbf{i}} & \begin{pmatrix} iM_1 \left[\frac{\mathbf{m}}{r} \partial_r + \frac{\mathbf{m}}{r^2} \right] \\ -iL'_1 \partial_r \frac{\mathbf{m}}{r} - i\Delta_2 \sigma_z \end{pmatrix} & \begin{pmatrix} -N'_2 \partial_r \partial_z + n_2 \varepsilon_{rz} \\ + i\Delta_3 \sigma_y \end{pmatrix} \hat{\mathbf{i}} \\ -\frac{imP_2}{r} & \begin{pmatrix} -iL'_1 \left[\frac{\mathbf{m}}{r} \partial_r + \frac{\mathbf{m}}{r^2} \right] \\ + iM_1 \partial_r \frac{\mathbf{m}}{r} + i\Delta_2 \sigma_z \end{pmatrix} & \begin{pmatrix} -M_1 \left[\partial_r^2 + \partial_r \frac{1}{r} \right] \\ + L'_1 \frac{\mathbf{m}^2}{r^2} - M_2 \partial_z^2 \\ + U_{v6} + m_1 \varepsilon_{rr} \\ + l_1 \varepsilon_{\phi\phi} + m_2 \varepsilon_{zz} \end{pmatrix} \hat{\mathbf{i}} & -iN'_2 \frac{\mathbf{m}}{r} \partial_z - i\Delta_3 \sigma_x \\ -\hat{\mathbf{i}} P_1 \partial_z & \begin{pmatrix} -N'_2 \left[\partial_r + \frac{1}{r} \right] \partial_z \\ + n_2 \varepsilon_{rz} - i\Delta_3 \sigma_y \end{pmatrix} \hat{\mathbf{i}} & -iN'_2 \frac{\mathbf{m}}{r} \partial_z + i\Delta_3 \sigma_x & \begin{pmatrix} -M_3 \left[\partial_r^2 + \frac{1}{r} \partial_r - \frac{\mathbf{m}^2}{r^2} \right] \\ -L'_2 \partial_z^2 + U_{v1} + l_2 \varepsilon_{zz} \\ + m_3 (\varepsilon_{rr} + \varepsilon_{\phi\phi}) \end{pmatrix} \hat{\mathbf{i}} \end{pmatrix}, \quad (58)$$

where $\partial_r^T = -(\partial_r + r^{-1})$ and the matrix \mathbf{m} has the form

$$\mathbf{m} = \begin{pmatrix} m - \frac{1}{2} & 0 \\ 0 & m + \frac{1}{2} \end{pmatrix}. \quad (59)$$

By identifying $\varepsilon_{rr} + \varepsilon_{\phi\phi} = \partial_r u_r + u_r/r + 2a$ (see Eqs. (17) and (18)) in cylindrical coordinates, we verified that the total strain dependent 8-band $\mathbf{k} \cdot \mathbf{p}$ Hamiltonian (58) in cylindrical coordinates is rotationally invariant with respect to the rotation around the z -axis.

IV. COMPUTATIONAL METHOD

We have used the Finite Element Method (FEM)³¹ and solve the corresponding eigenvalue problem of fully strain dependent 8-band $\mathbf{k} \cdot \mathbf{p}$ Hamiltonian in 3D Cartesian coordinates and in 2D cylindrical coordinates. For 3D solutions (both electromechanical and band structure calculations), we have imposed Neumann boundary conditions, i.e., the continuity equation must hold at the heterojunction which is also referred to as the internal boundaries. Dirichlet boundary conditions are imposed on the rest of the boundary. For cylindrically symmetric 2D model, we define the z axis to be perpendicular to the plane of the quantum-well layer and r axis that lies in the quantum-well plane. For electromechanical parts, we have imposed $u_r = 0$, $\partial_z u_z = 0$ and $\partial_z V = 0$ along the symmetry axis (i.e., at $r=0$) (for details, see Ref. 17). Here, we also impose Neumann boundary conditions at the internal boundaries and Dirichlet boundary conditions at the rest of the boundary. For the band structure calculations of 2D cylindrical nanowires, we have imposed

Neumann boundary conditions along the symmetry axis as well as at the internal boundaries. We have imposed Dirichlet boundary conditions at the rest of the boundary by assuming that the total Hamiltonian of the nanowire is rotationally invariant around z -direction. Finally, in 3D Cartesian coordinates and in 2D cylindrical coordinates, we have used the corresponding normalization conditions

$$\int_V |\Psi|^2 dx dy dz = 1, \quad (60)$$

$$\int_s |\Psi|^2 dr dz = 1. \quad (61)$$

The materials constants for our computation are taken from Refs. 16, 32, and 33 and listed in Tables I and II.

V. RESULTS AND DISCUSSIONS

We have plotted probability distributions of the ground and first excited states of electrons and holes in Figs. 1(a) and 1(b), respectively. Here, we consider the radius of the AlN/GaN/AlN nanowire as 20 nm. Also, in Figs. 2(a) and 2(b), we have plotted probability distributions of the ground and first excited states of electrons and holes where the radius of the AlN/GaN/AlN NWSLs was only 2 nm in order to investigate the radial influence of the localization of the electron and hole wavefunctions. By comparing the distribution functions of the ground state of electron in Fig. 1(a) for $R = 20$ nm and in Fig. 2(a) for $R = 2$ nm, we have found the maximum probability point at $(r, z) = (0, 0)$. However, for the excited states, we have found the zero probability point at $(r, z) = (0, 0)$ and maximum probability points at $(r, z) = (0, \pm 1.5)$. Also for hole states, we have found the

TABLE I. Lattice parameters of wurtzite GaN and AlN used in computation. If not indicated differently, they are taken from Ref. 33. The dependence of the material constants for $\text{Al}_x\text{Ga}_{1-x}\text{N}/\text{GaN}$ on positions x is derived from the empirical expression according to Ref. 33.

Parameter	GaN	AlN
a_0 (Å)	3.189	3.112
c_0 (Å)	5.185	4.982
c_{11} (GPa)	390	396
c_{12} (GPa)	145	137
c_{13} (GPa)	106	108
c_{33} (GPa)	398	373
c_{44} (GPa)	105	116
P_{sp} (C/m ²)	-0.034	-0.090
e_{31} (C/m ²)	-0.30 ^a	-0.25 ^a
e_{33} (C/m ²)	1.06 ^a	1.79 ^a
e_{15} (C/m ²)	0.33 ^a	0.42 ^a
κ_1	10.06 ^b	8.57 ^b
κ_2	9.28 ^b	8.67 ^b

^aReference 16.

^bReference 32.

maximum probability point at $(r, z) = (0, 0)$ for the ground state wavefunction in Fig. 1(b) ($R = 20$ nm) and zero probability point at $(r, z) = (0, 0)$ for the ground state wavefunction in Fig. 2(b) ($R = 2$ nm). However, for hole excited states, we have found the zero probability point at $(r, z) = (0, 0)$ and two zero probability points at $(r, z) = (0, \pm 1.5)$. In Fig. 3, we compare several eigenvalues of electron and hole states obtained from the 3D model in Cartesian coordinates to those values obtained from the 2D model in cylindrical coordinates. It can be seen that the eigenvalues obtained from the 3D and 2D models are in excellent agreement with difference less than 5%. The numerical error is due to the FEM implementation and can be reduced further by refining the mesh in 3D. This comparison of eigenvalues in 3D and 2D models demonstrates that the derived 8-band $\mathbf{k} \cdot \mathbf{p}$ model in cylindrical coordinates can be used for NWSLs instead of general 3D model. This substantially reduces the required computational time. Notice that for the holes in the valence band, the lowest state of $m = \pm 3/2$ corresponds to the ground state (see dashed line (red) in Fig. 3(b)) and the lowest state of $m = \pm 1/2$ corresponds to the first excited state (see solid line (black) in Fig. 3(b)). In Ref. 34, the Sercel-Vahala basis³⁵ was used for the model reductions in the case

TABLE II. Electron band structure parameters of wurtzite GaN and AlN used in computation. If not indicated differently, they are taken from Ref. 23. The dependence of the material constants for $\text{Al}_x\text{Ga}_{1-x}\text{N}/\text{GaN}$ on positions x is derived from the empirical expression according to Ref. 33.

Parameter	GaN	AlN
E_g (eV)	3.51	6.25
Δ_{cr} (eV)	0.034	-0.295
Δ_{so} (eV)	0.017 ^a	0.019 ^a
$m_{ }$	0.19 m_0	
m_{\perp}	0.21 m_0	
A_1	-5.947	
A_2	-0.528	
A_3	5.414	
A_4	-2.512	
A_5	-2.510	
A_6	-3.202	
A_7 (eV Å)	0.046	
P_1 (eV Å)	8.1	
P_2 (eV Å)	7.9	
a_1 (eV)	-4.9 ^a	-3.4 ^a
a_2 (eV)	-11.3 ^a	-11.8 ^a
D_1 (eV)	-3.7 ^a	-17.1 ^a
D_2 (eV)	4.5 ^a	7.9 ^a
D_3 (eV)	8.2 ^a	8.8 ^a
D_4 (eV)	-4.1 ^a	-3.9 ^a
D_5 (eV)	-4.0 ^a	-3.4 ^a
D_6 (eV)	-5.5 ^a	-3.4 ^a

^aReference 33.

of cylindrical coordinates. The methodology proposed in this paper is different. Based on Fig. 5, we further analyze the differences between these two approaches for NWSLs with small radii. Comparisons between 3D and 2D models are reported for the first time here for NWSLs, but the developed 8-band $\mathbf{k} \cdot \mathbf{p}$ model in cylindrical coordinates is applicable also to cylindrical quantum dots and other low dimensional nanostructures with cylindrical geometry as long as the systems are invariant around c-axis. In Fig. 4, we have plotted the probability distributions of ground and first excited states of electrons and holes in three layers of AlN/GaN NWSLs. We again have found that the maximum probability point for the ground state wavefunctions of electrons and holes is at $(r, z) = (0, 0)$.

In Fig. 5, we investigate the influence of piezoelectromechanical effects on the band structure calculations of

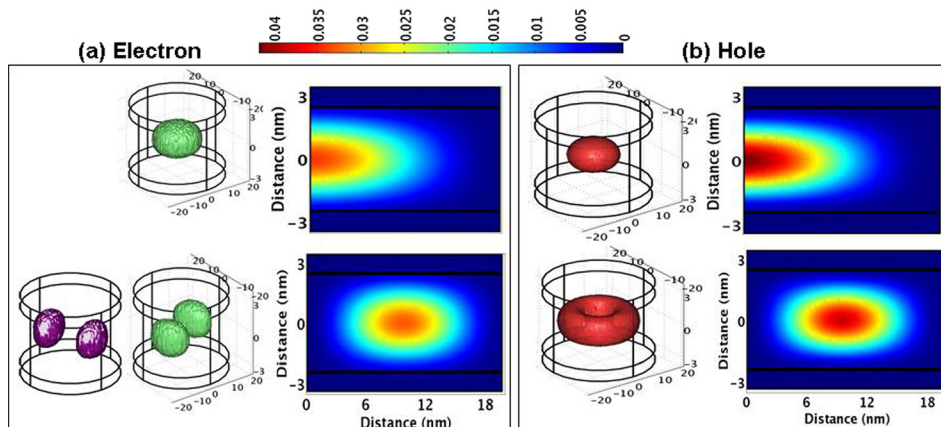


FIG. 1. Modeling of the distributions of electron and hole densities in AlN/GaN/AlN superlattice. Upper panel shows the ground state wavefunctions and lower panel shows the first excited state wavefunctions. First and third columns show the results of 3-dimensional modeling in Cartesian coordinates, while second and fourth columns show the results of 2-dimensional modeling in cylindrical coordinates. Notice that the first excited states of electrons in the conduction band are degenerate.

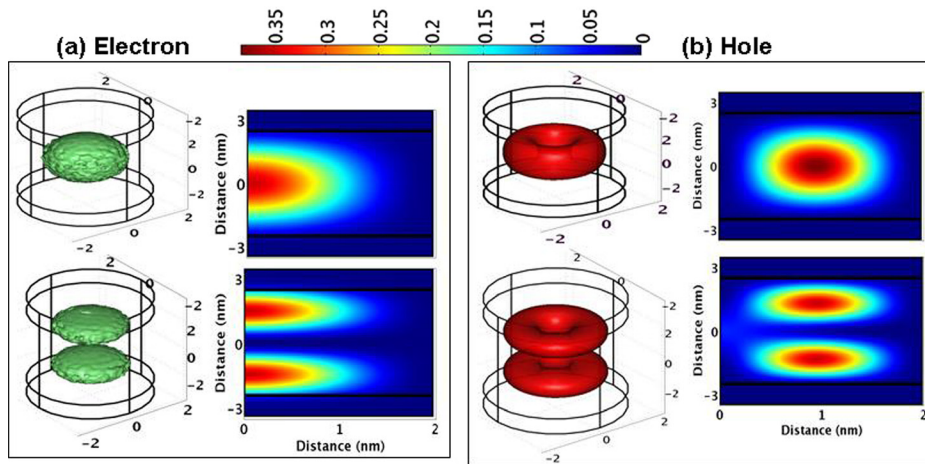


FIG. 2. Same as Fig. 1 but radius of the nanowire is chosen as 2 nm. By comparing Figs. 1 and 2, we clearly see the finite size effect on the localization of the distributions of electrons and holes wavefunctions.

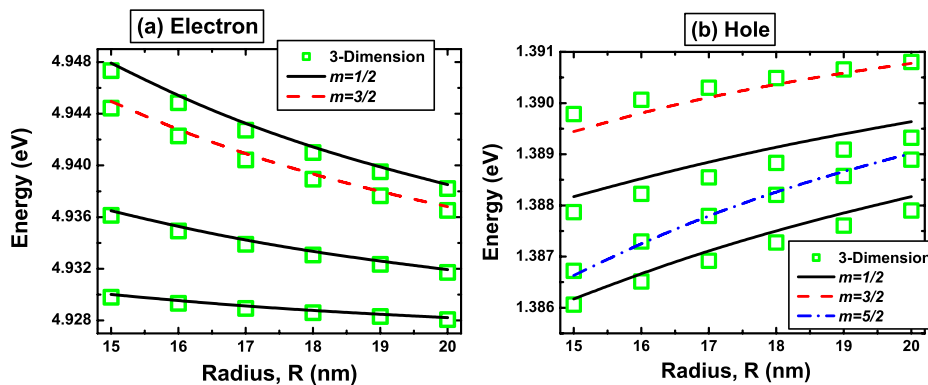


FIG. 3. Several energy eigenvalues of the lowest conduction and valence band states as a function of radius in a cylindrical AlN/GaN/AlN NWSLs. Eigenvalues obtained from the cylindrically symmetric 3-dimensional model in Cartesian coordinates are in excellent agreement with the 2-dimensional model in cylindrical coordinates.

electrons and holes in cylindrical AlN/GaN/AlN NWSLs (Figs. 5(a) and 5(b) present the results without and with piezoelectromechanical effects, respectively). We have substituted $m = \pm 1/2$ in Eq. (58) and found the ground, first, second, and so on excited states of electrons in the conduction bands. We confirm that for electrons in the conduction band, first excited states of $m = \pm 1/2$ correspond to the ground state of $m = \pm 3/2$ and second excited states of $m = \pm 1/2$ correspond to

the ground states of $m = \pm 5/2$, and so on. For holes in the valence band in Fig. 5(a), we demonstrate the finite radius influence at $R = 10$ nm where we find the crossing of the eigenstates between the lowest states of $m = 1/2$ and $m = 3/2$. This indicates that for $R < 10$ nm, the lowest state eigenvalue with $m = 1/2$ corresponds to the ground state and the lowest state eigenvalue with $m = 3/2$ corresponds to the first excited state. These results have not been previously reported.

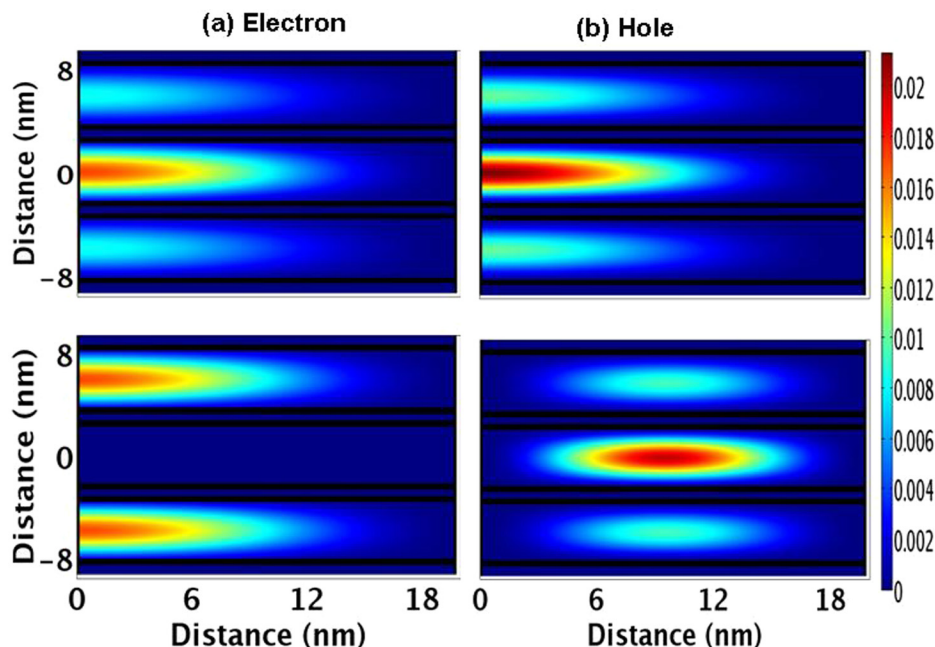


FIG. 4. Modeling of the distributions of electron and hole densities in three alternating layers of AlN/GaN superlattice. Upper panel shows the ground state wavefunctions and lower panel shows the first excited state wavefunctions.

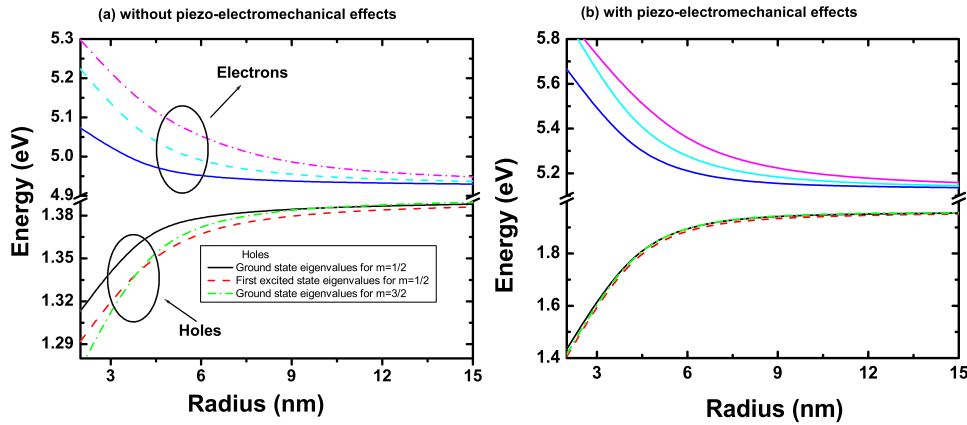


FIG. 5. Several energy eigenvalues of the lowest conduction and valence band states as a function of radius in 2-dimensional cylindrical AlN/GaN/AlN NWSLs.

In Fig. 6, we provide additional justification of utilizing 8-band $\mathbf{k} \cdot \mathbf{p}$ Hamiltonian in wide band gap AlN/GaN/AlN NWSLs. We compare the ground state eigenvalues obtained from the 8-band $\mathbf{k} \cdot \mathbf{p}$ Hamiltonian to those of decoupled 2-conduction and 6-valence bands envelope function methods. We see that the band structures of holes obtained from 6-bands and 8-bands $\mathbf{k} \cdot \mathbf{p}$ Hamiltonian both provide correct estimations. However, for electrons in the conduction band, the influence of non-parabolicity term (i.e., when including realistic values of P_1 and P_2) in the effective mass approximation in the 8-band $\mathbf{k} \cdot \mathbf{p}$ Hamiltonian induces a significant contribution to the band structure of wide band gap AlN/GaN/AlN NWSLs. By substituting $P_1 = P_2 = 0$ in (58), one can find decoupled 2-conduction and 6-valence band Hamiltonians. In Fig. 6(b), we have included the piezo-electromechanical effect and shown that the energy difference between the ground state eigenvalues of 2-band and 8-band enhanced. Further enhancement can be achieved if we bring the minima and maxima of the conduction and valence bands closer with the application of the gate controlled electric fields along z -direction.¹⁶

Bulk GaN and AlN have different lattice constants so when (0001) GaN NWSLs structure is grown, a significant lattice mismatch occurs at the interface between the GaN wells and AlN barriers.^{17,19,26} The strain induced polarization along z -direction results in strong piezoelectric fields and increased potentials along z -direction. We solve the Navier equations (1) for stress and Maxwell's equations (2) for piezoelectric fields in 3D on the one hand, and 2D coupled Eqs. (14), (15), and (16) in cylindrical coordinates

on the other hand, to investigate the piezo-electromechanical effects in wurtzite AlN/GaN/AlN (single layer of GaN) QWs. We assumed pseudomorphic strain conditions and plotted the nonvanishing position dependent strain tensor components (ϵ_{xx} , ϵ_{yy} , ϵ_{zz} , ϵ_{rr}) in Fig. 7(a) and electric field and potential in Fig. 7(b) as a function of position along the z -direction. In Fig. 8, we investigate the influence of piezo-electromechanical effects on the band structure calculation of wurtzite AlN/GaN NWSLs. We see that the influence of piezo-electromechanical effects pushes the minima of the conduction band at the top of the well and also pushes the maxima of the valence band at the bottom of the well. As a result, we find the localization of the electron wavefunction at the top of the well and hole wavefunction at the bottom of the well. In Fig. 9, we investigate the influence of piezo-electromechanical effects on the band structure calculation of wurtzite AlN/GaN multi layers of NWSLs. Here again, we see that the wavefunction of electrons in the conduction band is localized at the top of the GaN QW in the upper layer of the NWSLs and the hole wavefunction is localized at the bottom of the GaN QW in the lower layer of the NWSLs.

We now turn to another key result of the paper: critical radius and quantum confinement in wurtzite NWSL structures.

The critical radius ($R_c > R$) corresponds to those values of the radius of NWSLs for which the localization of the wavefunction penetrates into the barrier materials. For instance, if $R > R_c$, the localization of the wavefunction resides within the QW materials. In AlN/GaN NWSLs, the AlN barrier material acts as an infinite potential wall where

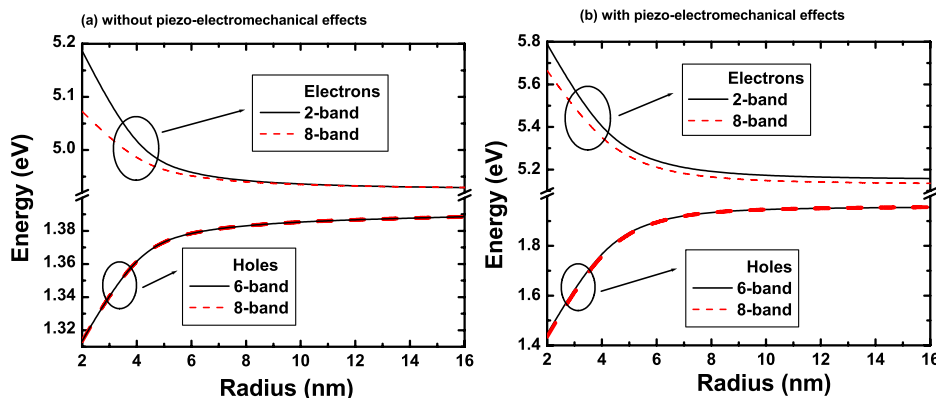


FIG. 6. Ground state energy eigenvalues vs radius of 2-dimensional cylindrical AlN/GaN/AlN NWSLs. Here, we compare the band structures of the NWSLs obtained from decoupled 2 conduction band and 6 valence band to that of 8-band $\mathbf{k} \cdot \mathbf{p}$ Hamiltonian. Here, we chose $m = 1/2$.

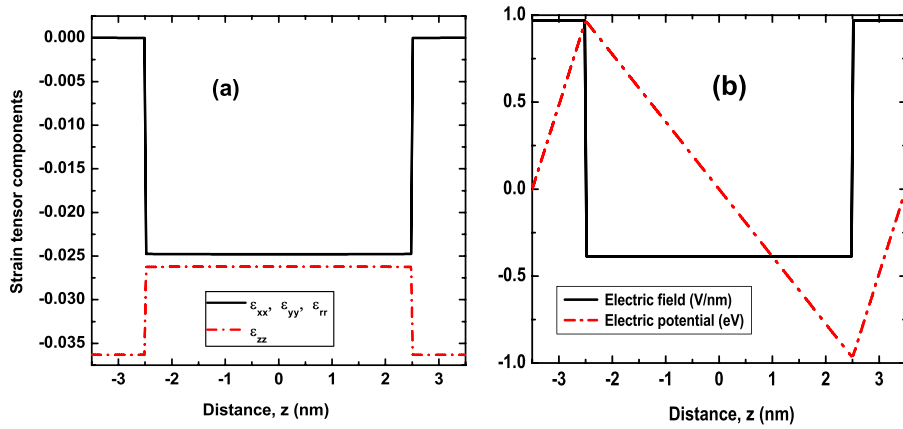


FIG. 7. (a) Strain tensor components for a AlN/GaN superlattice. (b) Piezoelectric field and piezoelectric potential for an AlN/GaN superlattice.

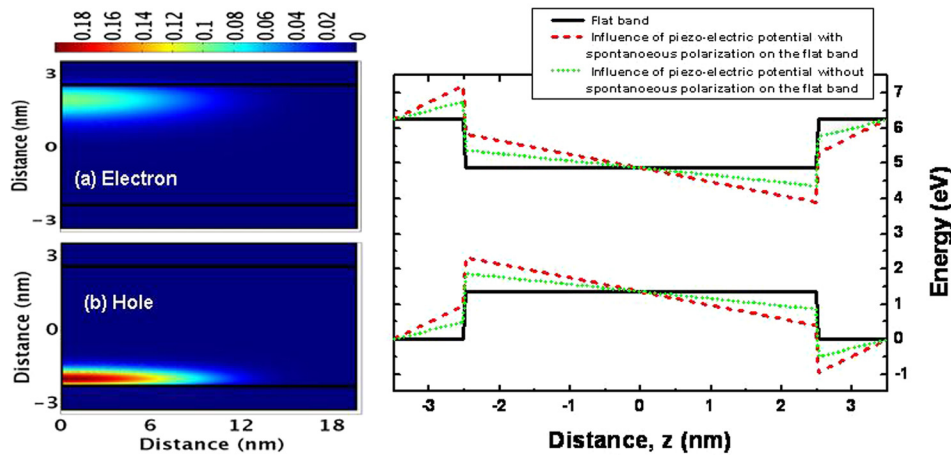


FIG. 8. Influence of piezo-electromechanical effects on the band structure calculations of wurtzite AlN/GaN superlattice.

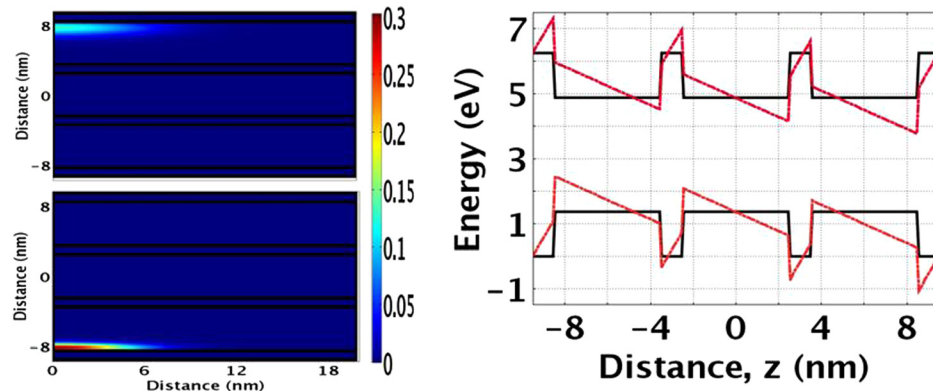


FIG. 9. Influence of piezo-electromechanical effects on the band structure calculations of wurtzite AlN/GaN superlattice.

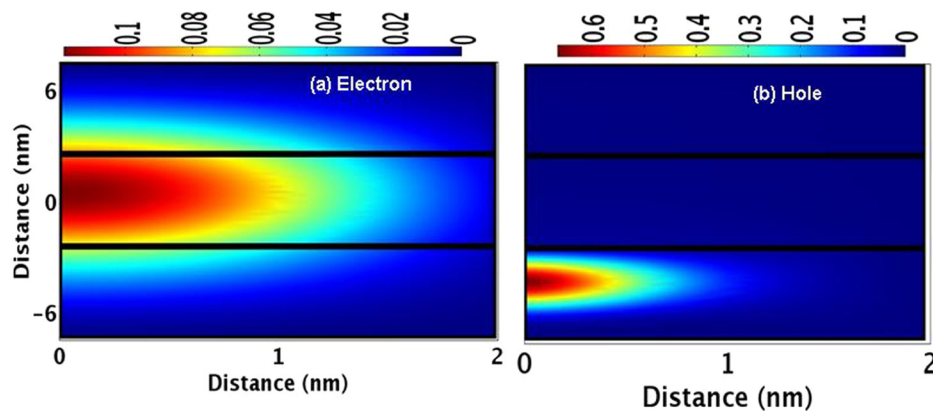


FIG. 10. Conduction band ground state (a) and valence band ground state (b) in symmetric $\text{Al}_x\text{Ga}_{1-x}\text{N}/\text{GaN}/\text{Al}_x\text{Ga}_{1-x}\text{N}$ NWSL structures with Al mole fraction $x = 0.01$. Notice that the wavefunctions spread into the barrier material which indicates that the barrier material acts as an inversion layer.

the penetration of the wavefunction into the barrier material is not possible. However, if we reduce the Al mole fraction in $\text{Al}_x\text{Ga}_{1-x}\text{N}/\text{GaN}$ NWSLs, we also reduce the band offsets, i.e., the barrier height of electrons (holes) is reduced at the interface of the heterojunction. In this situation, the influence of piezo-electromechanical effects is minimized and the penetration of electron (hole) wavefunctions can be seen to the barrier materials. In a simple one band model within the effective mass approximation, the authors in Ref. 11 provided the mathematical condition for the critical radius as

$$R \leq \left[\frac{m_B - m_w}{m_B m_w V_0} \right]^{1/2} j_{mn} = R_c, \quad (62)$$

where $j_{m,n}$ is the n th zero of the Bessel function, V_0 is the barrier height and m_B , m_w correspond to the effective masses of electron (hole) in the barrier and in the well. For $\text{Al}_x\text{Ga}_{1-x}\text{N}/\text{GaN}$ with $x=0.01$, we find $V_0 = 8.82$ meV, $m_B = 0.2109m_0$, and $m_w = 0.21m_0$ for electrons in the conduction band which gives $R_c = 6.3$ nm. In Fig. 10, we plotted the ground state wavefunction of electrons (Fig. 10(a)) and holes (Fig. 10(b)) in the conduction and valence bands, respectively, for the radius $R = 2$ nm $< R_c$. Notice that the wavefunctions of electrons and holes spread into the barrier materials ($\text{Al}_x\text{Ga}_{1-x}\text{N}/\text{GaN}$ with $x=0.01$). In Fig. 11, we plotted the energy level diagram of ground and first excited states of electrons and holes as a function of Al mole fraction. As we increase the Al mole fraction in $\text{Al}_x\text{Ga}_{1-x}\text{N}/\text{GaN}$ NWSLs, we also enhance the influence of piezo-electromechanical effects. As a result, the subband energy difference between ground and first excited states of electron (hole) states also increases.

Finally, in Fig. 12, we compare the band structures of $\text{AlN}/\text{GaN}/\text{AlN}$ NWSLs of cylindrical and square symmetry. We consider the volume of the square and cylindrical NWSLs to be the same (i.e., $a = \sqrt{\pi}R$, where a is the side length of the square NWSLs and R is the radius of the cylindrical NWSLs). For smaller values of R or a , the localized states are formed very close to the edge and thus we find the larger eigenvalues for the NWSLs of square symmetry.

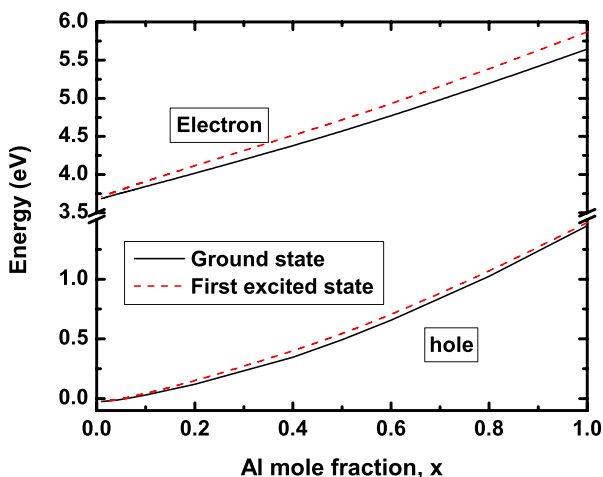


FIG. 11. Subband energy levels of electrons and holes vs Al mole fraction in symmetric $\text{Al}_x\text{Ga}_{1-x}\text{N}/\text{GaN}/\text{Al}_x\text{Ga}_{1-x}\text{N}$ NWSL structures.

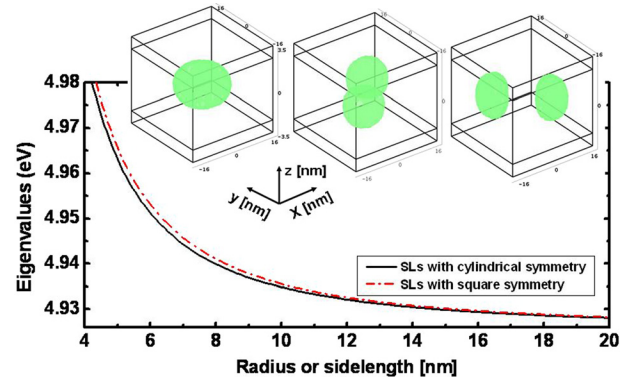


FIG. 12. Ground state eigenvalues vs radius of cylindrical NWSLs or side-length of square NWSLs. Notice that the localization of first excited state wavefunction in square symmetry (inset plot) is different than for the case in cylindrical symmetry (Fig. 1(a) lower panel).

However, for larger values of R or a , the localized states are formed far away from the edge in both types of cylindrical and square NWSLs and thus we find the eigenvalues are not substantially influenced by the choice of either square or cylindrical symmetry. In this case, the localization of first excited state wavefunction with square symmetry (inset plot of Fig. 12) is different from the case with cylindrical symmetry (Fig. 1(a) lower panel) which might indicate that the symmetry is broken in square shape NWSLs.

VI. CONCLUSIONS

By applying rotationally invariant basis functions with appropriate unitary transformation, we have formulated and applied the strain dependent 8-band $\mathbf{k} \cdot \mathbf{p}$ Hamiltonian in cylindrical coordinates. This approach allows us to find the band structures of low dimensional semiconductor nanostructures in a computationally efficient way. This includes quantum dots, quantum wells, or nanowire superlattices as long as the systems are cylindrically symmetric along z -direction. We have provided the detailed analysis of the eigenvalues of electron (hole) states of wurtzite NWSLs for both 3D (Cartesian coordinates) and 2D (cylindrical coordinates) models. In a single and vertically stacked multiple layer of NWSLs, we have shown that the piezo-electromechanical effects push the electron wavefunction to the top of quantum well, while they push the hole wavefunction to the bottom of the well. We have shown that the influence of piezo-electromechanical effects in $\text{Al}_x\text{Ga}_{1-x}\text{N}/\text{GaN}$ structures can be minimized by varying the Al mole fraction. In a situation, where the radius of the NWSL is very small compared to the critical radius, the localization of the electron (hole) wavefunction spreads into the barrier material. In this case, the barrier materials act as an inversion layer. Finally, we have shown that the edge of the square symmetry enhances the eigenvalues of the localized states for smaller values of the side length of the square NWSLs. For large NWSLs, we have shown that the eigenvalues of the localized states of square and cylindrical NWSLs are not substantially influenced by the edge states but the localization of wavefunction with square symmetry is different from the case

with cylindrical symmetry which might indicate that the symmetry is broken in square shape NWSLs.

ACKNOWLEDGMENTS

The authors acknowledge Dr. Sunil Patil for his input on the initial version of this paper. This work was supported by Natural Sciences and Engineering Research Council (NSERC) of Canada and Canada Research Chair (CRC) programs.

- ¹Y. Huang, X. Duan, Y. Cui, L. J. Lauhon, K.-H. Kim, and C. M. Lieber, "Logic gates and computation from assembled nanowire building blocks," *Science* **294**, 1313–1317 (2001).
- ²Y.-M. Lin and M. S. Dresselhaus, "Thermoelectric properties of superlattice nanowires," *Phys. Rev. B* **68**, 075304 (2003).
- ³R. Venkatasubramanian, E. Siivola, T. Colpitts, and B. O'Quinn, "Thin-film thermoelectric devices with high room-temperature figures of merit," *Nature* **413**, 597 (2001).
- ⁴T. C. Harman, P. J. Taylor, M. P. Walsh, and B. E. LaForge, "Quantum dot superlattice thermoelectric materials and devices," *Science* **297**, 2229–2232 (2002).
- ⁵K. Nielsch, R. B. Wehrspohn, J. Barthel, J. Kirschner, U. Gösele, S. F. Fischer, and H. Kronmüller, "Hexagonally ordered 100 nm period nickel nanowire arrays," *Appl. Phys. Lett.* **79**, 1360–1362 (2001).
- ⁶S. Prabhakar, R. V. Melnik, P. Neittaanmäki, and T. Tiihonen, "Coupled magneto-thermo-electromechanical effects and electronic properties of quantum dots," *J. Comput. Theor. Nanosci.* **10**, 534–547 (2013).
- ⁷Y. Huang, X. Duan, Y. Cui, and C. M. Lieber, "Gallium nitride nanowire nanodevices," *Nano Lett.* **2**, 101–104 (2002).
- ⁸L. C. Chuang, M. Moewe, C. Chase, N. P. Kobayashi, C. Chang-Hasnain, and S. Crankshaw, "Critical diameter for iii-v nanowires grown on lattice-mismatched substrates," *Appl. Phys. Lett.* **90**, 043115 (2007).
- ⁹G. E. Cirlin, V. G. Dubrovskii, I. P. Soshnikov, N. V. Sibirev, Y. B. Samsonenko, A. D. Bouravleuv, J. C. Harmand, and F. Glas, "Critical diameters and temperature domains for MBE growth of III-V nanowires on lattice mismatched substrates," *Phys. Status Solidi (RRL)* **3**, 112–114 (2009).
- ¹⁰S. Raychaudhuri and E. T. Yu, "Critical dimensions in coherently strained coaxial nanowire heterostructures," *J. Appl. Phys.* **99**, 114308 (2006).
- ¹¹L. C. L. Y. Voon, B. Lassen, R. Melnik, and M. Willatzen, "Prediction of barrier localization in modulated nanowires," *J. Appl. Phys.* **96**, 4660–4662 (2004).
- ¹²M. Willatzen, R. Melnik, C. Galeriu, and L. L. Y. Voon, "Quantum confinement phenomena in nanowire superlattice structures," *Math. Comput. Simul.* **65**, 385–397 (2004).
- ¹³L. C. L. Y. Voon and M. Willatzen, "Electron states in modulated nanowires," *J. Appl. Phys.* **93**, 9997–10000 (2003).
- ¹⁴B. Lassen, M. Willatzen, D. Baretin, R. V. N. Melnik, and L. C. L. Y. Voon, "Electromechanical effects in electron structure for GaN/AlN quantum dots," *J. Phys.: Conf. Ser.* **107**, 012008 (2008).
- ¹⁵R. V. N. Melnik, "Generalised solutions, discrete models and energy estimates for a 2D problem of coupled field theory," *Appl. Math. Comput.* **107**, 27 (2000).
- ¹⁶S. Prabhakar, R. V. Melnik, P. Neittaanmäki, and T. Tiihonen, "Coupled electromechanical effects in wurtzite quantum dots with wetting layers in gate controlled electric fields: The multiband case," *Physica E (Amsterdam)* **46**, 97–104 (2012).
- ¹⁷D. Baretin, B. Lassen, and M. Willatzen, "Electromechanical fields in GaN/AlN wurtzite quantum dots," *J. Phys.: Conf. Ser.* **107**, 012001 (2008).
- ¹⁸S. Prabhakar and R. Melnik, "Influence of electromechanical effects and wetting layers on band structures of AlN/GaN quantum dots and spin control," *J. Appl. Phys.* **108**, 064330 (2010).
- ¹⁹S. R. Patil and R. V. N. Melnik, "Thermoelectromechanical effects in quantum dots," *Nanotechnology* **20**, 125402 (2009).
- ²⁰E. O. Kane, "Band structure of indium antimonide," *J. Phys. Chem. Solids* **1**, 249 (1957).
- ²¹G. Bir and G. Pikus, *Symmetry and Strain Induced Effects in Semiconductors* (Wiley, 1974).
- ²²P.-O. Löwdin, "A note on the quantum-mechanical perturbation theory," *J. Chem. Phys.* **19**, 1396 (1951).
- ²³P. Rinke, M. Winkelkemper, A. Qteish, D. Bimberg, J. Neugebauer, and M. Scheffler, "Consistent set of band parameters for the group-iii nitrides AlN, GaN, and InN," *Phys. Rev. B* **77**, 075202 (2008).
- ²⁴J. Y. Fu and M. W. Wu, "Spin-orbit coupling in bulk ZnO and GaN," *J. Appl. Phys.* **104**, 093712 (2008).
- ²⁵M. Winkelkemper, A. Schliwa, and D. Bimberg, "Interrelation of structural and electronic properties in $\text{In}_x\text{Ga}_{1-x}\text{N}/\text{GaN}$ quantum dots using an eight-band $k \cdot p$ model," *Phys. Rev. B* **74**, 155322 (2006).
- ²⁶S. L. Chuang and C. S. Chang, " $k \cdot p$ method for strained wurtzite semiconductors," *Phys. Rev. B* **54**, 2491 (1996).
- ²⁷V. A. Fonoberov and A. A. Balandin, "Excitonic properties of strained wurtzite and zinc-blende $\text{GaN}/\text{Al}_x\text{Ga}_{1-x}\text{N}$ quantum dots," *J. Appl. Phys.* **94**, 7178 (2003).
- ²⁸S. Prabhakar, E. Takhtamirov, and R. Melnik, "Coupled multi-physics models for the analysis of the conduction and valence band eigenenergies in cylindrical quantum dots," *Acta Phys. Pol. A* **121**, 85 (2012).
- ²⁹E. Takhtamirov and R. Melnik, "Cylindrical coordinates representation for valence-band and Kane Hamiltonians for wurtzite and zinc-blende heterostructures," e-print [arXiv:1107.1285v1](https://arxiv.org/abs/1107.1285v1).
- ³⁰L. C. L. Y. Voon, C. Galeriu, B. Lassen, M. Willatzen, and R. Melnik, "Electronic structure of wurtzite quantum dots with cylindrical symmetry," *Appl. Phys. Lett.* **87**, 041906 (2005).
- ³¹Comsol Multiphysics version 3.5a, see <http://www.comsol.com>.
- ³²S. M. Komirenko, K. W. Kim, M. A. Strosio, and M. Dutta, "Dispersion of polar optical phonons in wurtzite quantum wells," *Phys. Rev. B* **59**, 5013 (1999).
- ³³I. Vurgaftman and J. R. Meyer, "Band parameters for nitrogen-containing semiconductors," *J. Appl. Phys.* **94**, 3675 (2003).
- ³⁴L. C. Lew Yan Voon, R. Melnik, B. Lassen, and M. Willatzen, "Influence of aspect ratio on the lowest states of quantum rods," *Nano Lett.* **4**, 289–292 (2004).
- ³⁵P. C. Sercel and K. J. Vahala, "Analytical formalism for determining quantum-wire and quantum-dot band structure in the multiband envelope-function approximation," *Phys. Rev. B* **42**, 3690–3710 (1990).